6

Modeling Solidification Phenomena in the Continuous Casting of Carbon Steels

Panagiotis Sismanis
SIDENOR SA
Greece

1. Introduction

In recent years the quest for advanced steel quality satisfying more stringent specifications by time has forced research in the development of advanced equipment for the improvement of the internal structure of the continuously cast steels. A relatively important role has played the better understanding of the solidification phenomena that occur during the final stages of the solidification. Dynamic soft-reduction machines have been placed in industrial practice with top-level performance. Nevertheless, the numerical solution of the governing heat-transfer differential equation under the proper initial and boundary conditions continues to play the paramount role for the fundamental approach of the whole solidification process. Steel properties are critical upon the solidification behaviour. Different chemical analyses of carbon steels alter the solidus and liquidus temperatures and therefore influence the calculated results. Shell growth, local cooling rates and solidification times, solid fraction, and secondary dendrite arm-spacing are some important metallurgical parameters that need to be ultimately computed for specific steel grades once the heat transfer problem is solved.

2. Previous work and current status

Solidification heat-transfer has been extensively studied throughout the years and there are numerous works on the subject in the academic and industrial fields. Towards the development of continuous casting machines adapted to the needs of the various steel grades a great deal of research work has been published in this metallurgical domain. In one of the early works (Mizikar, 1967), the fundamental relationships and the means of solution were described, but in a series of articles (Brimacombe, 1976) and (Brimacombe et al, 1977, 1978, 1979, 1980) some important answers to the heat transfer problem as well as to associated product internal structures and continuous-casting problems were presented in detail. The crucial knowledge-creation practice of combining experiments and models together was the main method applied to most of these works. In this way, the shell thickness at mold exit, the metallurgical length of the caster, the location down the caster where cracks initiate, and the cooling practice below the mold to avoid reheating cracks were some of the points addressed. At that time, the first finite-element thermal-stress models of solidification were applied in order to understand the internal stress distribution in the solidifying steel strand below the mold. The need for data with respect to the

mechanical properties of steels and specifically creep at high temperatures as a means for controlling the continuous casting events was realized from the early years of analysis (Palmaers, 1978). In a similar study, the bulging produced by creep in the continuously cast slabs was analyzed (Grill & Schwerdtfeger, 1979) with a finite-element model. In order to simulate the unbending process in a continuous casting machine a multi-beam model was proposed (Tacke, 1985) for strand straightening in the caster. With the advent of the computer revolution more advanced topics relevant to the fluid flow in the mold were addressed. Unsteady-state turbulent phenomena in the mold were tackled using the large eddy simulation method of analysis (Sivaramakrishnan et al, 2000); in extreme cases, it was reported that the computer program could take up to a month to converge and come up with a solution. Nevertheless, computational heat-transfer programs have helped in the development of better internal structure continuously-cast steels mostly for two main reasons: [1] the online control of the casting process and, [2] the offline analysis of factors which are more intrinsic to the specific nature of a steel grade under investigation, i.e., chemical analysis and internal structure. Continuing the literature survey more focus will be given to selected published works relevant to the second [2] influential reason.

The formation of internal cracks that influence the internal structure of slabs was investigated from the early years (Fuji et al, 1976) of continuous casting. It was proven that internal cracks are formed adjacent to the solid-liquid interface and greatly influenced by bulging. As creep was critical upon bulging in continuously cast slabs a model was proposed (Fujii et al, 1981) with adequate agreement between theory and practice for low and medium carbon aluminum-killed steels. In another study (Matsumiya et al, 1984) a mathematical analysis model was established in order to investigate the interdendritic micro-segregation using a finite difference scheme and taking into consideration the diffusion of a solute in the solid and liquid phases. As mechanical behavior of plain carbon steel in the austenite temperature region was proven of paramount importance in the continuous casting process a set of simple constitutive equations was developed (Kozlowski et al, 1992) for the elastoplastic analysis used in finite element models. Chemical composition of steel and specifically equivalent carbon content as well as the Mn/S ratio were found to define a critical strain value above which internal structure problems could appear (Hiebler et al, 1994). As analysis deepened into the internal structure and specifically into micro- and macro-segregation, relationships between primary and secondary dendrite arm spacing (Imagumbai, 1994) started to appear. In fact, first order analysis revealed that secondary dendrite arm-spacing is about one-half of the primary one. The effect of cooling rate on zero-strength-temperature (ZST) and zero-ductility-temperature (ZDT) was found to be significant (Won et al, 1998) due to segregation of solute elements at the final stage of solidification. The calculated temperatures at the solid fractions of 0.75 and 0.99 corresponded to the experimentally measured ZST and ZDT, respectively. Furthermore, a set of relationships that take under consideration steel composition, cooling rate, and solid fraction was proposed; the suggested prediction equation on ZST and ZDT was found in relative agreement with experimental results. In a monumental work (Cabrera-Marrero et al, 1998), the dendritic microstructure of continuously-cast steel billets was analyzed and found in agreement with experimental results. In fact, the differential equation of heat transfer was numerically solved along the sections of the caster and local solidification times related to microstructure for various steel compositions were computed. Based on the Clyne-Kurz model a simple model of micro-segregation during solidification of steels was developed

(Won & Thomas, 2001). In this way, the secondary dendrite arm spacing can be sufficiently computed with respect to carbon content and local cooling rates. In another study (Han et al, 2001), the formation of internal cracks in continuously cast slabs was mathematically analyzed with the implementation of a strain analysis model together with a micro-segregation model. The equation of heat transfer was also numerically solved along the caster. Total strain based on bulging, unbending, and roll-misalignment attributed strains, was computed and checked against the critical strain. Consequently, internal structure problems could be identified and verified in practice. The unsteady bulging was found to be (Yoon et al, 2002) the main reason of mold level hunching during thin slab casting. A finite difference scheme for the numerical solution of the heat transfer equation together with a continuous beam model and a primary creep equation were developed in order to match experimental data. A 2D unsteady heat-transfer model (Zhu et al, 2003) was applied to obtain the surface temperature and shell thickness of continuous casting slabs during the process of solidification. Roll misalignment was proven to provoke internal cracks once total strain at the solid/liquid interface exceeded the critical strain for the examined chemical composition of steel slabs. As creep was proven to be important in the continuous casting of steels, an evaluation of common constitutive equations was performed (Pierer at al, 2005) and tested against experimental data. The proposed results could help in the development of more sophisticated 2D finite element models. Once offline computer models are proven correct they can be applied online in real-time applications and minimize internal defects (Ma et al, 2008).

Consequently, very advanced types of continuous casting machines have appeared in the international market as a result of these investigations. Different steel grades are classified into groups which are processed in the continuous casters as heats cast with similar design and operating parameters. Automation plays an important role supervising the whole continuous casting process by running in two levels, i.e., controlling the process, and computing the final solidification front as a real-time solution to the heat-transfer problem case. The numerous steel products of excellent quality manifest the success of these sophisticated casting machines.

3. Present work

In this work the modelling of the solidification phenomena for two slab casters installed in different plants, one in Stomana, Pernik, Bulgaria, and the other in Sovel, Almyros, Greece, is presented. Both plants belong to the SIDENOR group of companies. Simple design and operating parameters together with the chemical analyses of the steel grades cast are the basic data to approximate the heat transfer solution, compute the temperature distributions inside the continuously cast slabs in every section of the caster, and investigate the solidification phenomena from the metallurgical point of view. A 3D numerical solution of the differential equation of heat transfer was developed and tested in a previous publication (Sismanis, 2010) and is not to be presented in detail here. Some routines were also implemented in the main core of that developed software in order to cover the extra computational work required for the metallurgical analysis of the solidification phenomena. Furthermore, strain analysis for any slab bulging and for the straightening positions was implemented as well. The methodology applied for tackling the continuous casting problem for different carbon steel grades from the metallurgical point of view is maybe

what makes this purely computational study more intriguing and specific in nature. Critical formulas that bind the heat transfer problem with the various solidification parameters and strains in the slab are presented and discussed.

3.1 The heat transfer model applied

The general 3D heat transfer equation that describes the temperature distribution inside the solidifying body is given by the following equation (Carslaw & Jaeger, 1986) and (Incropera & DeWitt, 1981):

$$\rho C_P \frac{\partial T}{\partial t} = \nabla \cdot k \nabla T + S \tag{1}$$

The source term S, in units $W \cdot m^{-3}$, may be considered (Patankar, 1980) to be of the form:

$$S = S_C + S_P \cdot T \tag{2}$$

that is, by a constant term and a temperature dependent term and can be related to correspond to the latent heat of phase change. Furthermore, T is the temperature, and ρ, C_p, and k are the density, heat capacity, and thermal conductivity of steel, respectively. The heat transfer equation in Cartesian coordinates may be written as:

$$\rho C_p \frac{\partial T}{\partial t} = \frac{\partial}{\partial x}\left(k \frac{\partial T}{\partial x}\right) + \frac{\partial}{\partial y}\left(k \frac{\partial T}{\partial y}\right) + \frac{\partial}{\partial z}\left(k \frac{\partial T}{\partial z}\right) + S \tag{3}$$

The solidification problem in the continuous casting may be considered as such of studying the advance of the solidification front by means of mathematical solution of the global heat transfer involved in the specific geometry, and the local heat transfer in the mushy zone. In the present study, the heat conduction along the casting direction is considered to be negligible. So, (3) can be written as:

$$\rho C_P \frac{\partial T}{\partial t} = \frac{\partial}{\partial x}\left(k \frac{\partial T}{\partial x}\right) + \frac{\partial}{\partial y}\left(k \frac{\partial T}{\partial y}\right) + S \tag{4}$$

The boundary conditions applied in order to solve (4) are as follows:
Heat flux in the mold is equalized to the empirical equation used by other researchers (Lait et al, 1974),

$$q_m = 2.67 \times 10^6 - 2.21 \times 10^5 \sqrt{t_d} \tag{5}$$

The mold heat-flux (q_m) is given in W/m^2, and t_d (in seconds) is the dwell time of the strand inside the mold. Involving an expression for the local heat-transfer coefficient inside the mold (Yoon et al, 2002) a more realistic formula was derived that exhibited good results in the present study:

$$h_m = 1.35 \cdot 10^{-3} \cdot (1 - 0.8z) \cdot q_m \tag{6}$$

The heat fluxes due to water spraying and radiation of the strand in the secondary cooling zones were calculated using the following expressions:

$$q_s = h_s \cdot (T - T_{w0}) \tag{7}$$

$$q_r = h_r \cdot (T - T_{env}) \quad with \quad h_r = \sigma\varepsilon \cdot \frac{T^4 - T_{env}^{\ 4}}{T - T_{env}} \tag{8}$$

$$q_c = h_c \cdot (T - T_{env}) \tag{9}$$

where h_s, h_r, and h_c are the heat transfer coefficients for spray cooling, radiation, and convection, respectively, T_{w0} is the water temperature, T_{env} is the ambient temperature, σ is the Stefan-Boltzmann constant, and ε is the steel emissivity (equal to 0.8 in the present study). Natural convection was assumed to prevail at the convection heat transfer as stagnant air-flow conditions were considered due to the low casting speeds of the strand applied in practice. The strand was assumed to be a long horizontal cylinder with an equivalent diameter of a circle having the same area with that of the strand cross-sectional area, and a correlation valid for a wide Rayleigh number range proposed by (Churchill & Chu, 1975) was applied, written in the form proposed by (Burmeister, 1983):

$$\sqrt{Nu_D} = 0.60 + 0.387B^{1/6} \qquad B = Ra_D\left[1 + \left(\frac{0.559}{\mathrm{Pr}}\right)^{9/16}\right]^{16/9} \qquad (10^{-5} < B < 10^{13}) \tag{10}$$

where Nu, Ra, and Pr are the dimensionless Nusselt, Rayleigh, and Prandtl numbers, respectively. In this way, h_c is calculated by means of the Nu_D number. It is worth mentioning, however, that the radiation effects are more pronounced than the convection ones in the continuous casting of steels. From various expressions proposed in the literature for the heat transfer coefficient in water-spray cooling systems the following formula was applied as approaching the present casting conditions:

$$h_s = 1570 \cdot W^{0.55} \cdot \frac{1 - 0.0075T_{w0}}{4} \tag{11}$$

where W is the water flux for any secondary spray zone in liters/m^2/sec, and h_s is in W/m^2/K. At any point along the secondary zones (starting just below the mold) of the caster the total flux q_{tot} is computed according to the following formula, taking into account that q_s may be zero at areas where no sprays are applied:

$$q_{tot} = q_s + q_r + q \tag{12}$$

In mathematical terms, considering a one-fourth of the cross-section of a slab assuming perfect symmetry, the aforementioned boundary conditions can be written as:

$$-k\frac{\partial T}{\partial x} = \begin{cases} q_m \ \ at\ x = W_x,\ 0 \le y \le W_y,\ 0 \le z \le L_m \\ q_{tot}\ at\ x = W_x,\ 0 \le y \le W_y,\ z > L_m \end{cases} \tag{13}$$

$$-k\frac{\partial T}{\partial y} = \begin{cases} q_m \ \ at\ y = W_y,\ 0 \le x \le W_x,\ 0 \le z \le L_m \\ q_{tot}\ at\ y = W_y,\ 0 \le x \le W_x,\ z > L_m \end{cases} \tag{14}$$

where z follows the casting direction starting from the meniscus level inside the mold; consequently, the mold has an active length of L_m. W_x and W_y are the half-width and the half-thickness of the cast product, respectively. Due to symmetry, the heat fluxes at the central planes are considered to be zero:

$$-k\frac{\partial T}{\partial x}=0 \; at \; x=0,\; 0\le y\le W_y,\; z\ge 0 \tag{15}$$

$$-k\frac{\partial T}{\partial y}=0 \; at \; y=0,\; 0\le x\le W_x,\; z\ge 0 \tag{16}$$

Finally, the initial temperature of the pouring liquid steel is supposed to be the temperature of liquid steel in the tundish:

$$T=T_0 \text{ at } t=0 \text{ (and } z=0),\; 0<x<W_x,\; 0<y<W_y \tag{17}$$

The thermo-physical properties of carbon steels were obtained from the published work of (Cabrera-Marrero et al, 1998); the properties were given as functions of carbon content for the liquid, mushy, solid, and transformation temperature domain values. The liquidus and solidus temperatures were obtained from the work of (Thomas et al, 1987):

$$\begin{aligned} T_L = {} & 1537-88(\%C)-8(\%Si)-5(\%Mn)-30(\%P)-25(\%S) \\ & -4(\%Ni)-1.5(\%Cr)-5(\%Cu)-2(\%Mo)-2(\%V)-18(\%Ti) \end{aligned} \tag{18}$$

$$\begin{aligned} T_S = {} & 1535-200(\%C)-12.3(\%Si)-6.8(\%Mn)-124.5(\%P)-183.9(\%S) \\ & -4.3(\%Ni)-1.4(\%Cr)-4.1(\%Al) \end{aligned} \tag{19}$$

At any time step the simulating program computes whether a given nodal point is at a lower or higher temperature than the liquidus or solidus temperatures for a given steel composition. Consequently, the instantaneous position of the solidification front is derived, and therefore, in the solidification direction the last solidified nodal point at the solidus temperature.

3.1.1 Strain analysis computations

Bulging strain ε_B was computed based on the analysis by (Fujii et al, 1976) in which primary creep was taken under consideration. Equations (20) through (27) contain the necessary formulas used in these computations:

$$\varepsilon_B = 1600\cdot\delta_B\cdot S/\ell_P{}^2 \tag{20}$$

$$\delta_B=\beta\sqrt{t_P}\;/S^3 \quad and \quad t_P=\ell_P/u_C \tag{21}$$

$$\beta=12(1-\nu^2)\cdot\sigma_P\cdot\alpha_5\cdot A_0\cdot\ell_P{}^4 \tag{22}$$

$$\alpha_5=\frac{2}{\pi^5\cosh(\psi)}\left\{2\cosh(\psi)-\psi\tanh(\psi)-2\right\} \qquad and \qquad \psi=\frac{\pi W_x}{\ell_P} \tag{23}$$

Some important parameters are included in the expressions: ℓ_P is the roll pitch in the part of the caster under consideration, u_C is the casting speed, t_P is time in seconds, S is the thickness of the solidified shell at the point of analysis along the caster, and ν is the Poisson ratio for steel which is related to steel according to the following relationship (Uehara et al, 1986):

$$\nu = 0.278 + 8.23 \times 10^{-5} \cdot T_P \quad and \quad T_P = \frac{1}{2}\left(T_S + T_{Surf}\right) \tag{24}$$

The T_P value (in ^oC) is taken as the average value between the solidus and the surface temperature of the slab. Primary creep data were taken from the work of (Palmaers, 1978) and applied with good results mostly for low and medium carbon steel slabs produced at Sovel. Table 1 presents the data used. Equation (25) illustrates the expression used for the calculation of the primary creep strain and σ_P (in MPa) resembles the ferro-static pressure (26) at a point along the caster which has a distance H_5 measured along the vertical axis from the meniscus level; it is clarified that the maximum value of H_5 can be around the caster radius (27).

$$\varepsilon_C = A_0 \cdot {\sigma_P}^n \cdot {t_P}^m \cdot \exp(-\frac{Q_C}{RT}) \tag{25}$$

$$\sigma_P = \rho g H_5 \tag{26}$$

$$H_{5,\max} = R_C \tag{27}$$

For the steel slabs produced at Stomana, the constitutive equations for model II (Kozlowski et al, 1992) were applied after integration (T in Kelvin=T_P+273.16):

$$\dot{\varepsilon}_P = C \cdot \exp(-Q_{C,K} / T) \cdot {\sigma_P}^n \cdot {t_P}^m \tag{28}$$

where, $Q_{C,K}$ = 17160 and:

$$C = 0.3091 + 0.2090 \cdot (\%C) + 0.1773 \cdot (\%C)^2 \tag{29}$$

$$n = 6.365 - 4.521 \cdot 10^{-3} \cdot T + 1.439 \cdot 10^{-6} \cdot T^2 \tag{30}$$

$$m = -1.362 + 5.761 \cdot 10^{-4} \cdot T + 1.982 \cdot 10^{-8} \cdot T^2 \tag{31}$$

So, after appropriate integration of the strain rate (28), the following expression was applied for the primary creep that exhibited better results than the correlations of (Palmaers, 1978) specifically for the Stomana slabs, probably due to their much larger size compared to the size of the slabs produced at Sovel:

$$\varepsilon_P = \left(C / (m+1)\right) \cdot \exp(-Q_{C,K} / T) \cdot {\sigma_P}^n \cdot t^{m+1} \tag{32}$$

The unbending strain was computed according to equation (33) where R_{n-1}, R_n are the unbending radii of the caster, (Uehara et al, 1986) and (Zhu et al, 2003).

$$\varepsilon_S = 100 \cdot (W_y - S) \cdot \left| \frac{1}{R_{n-1}} - \frac{1}{R_n} \right| \tag{33}$$

Any caster misalignment of value δ_M can be computed according to (34), as described in the works of (Han et al, 2001) and (Zhu et al, 2003):

$$\varepsilon_M = 300 \cdot S \cdot \delta_M / \ell_P{}^2 \tag{34}$$

The total strain ε_{tot} that a slab may undergo at a specific point along the caster is the sum of all the aforementioned strains:

$$\varepsilon_{tot} = \varepsilon_B + \varepsilon_S + \varepsilon_M \tag{35}$$

The total strain should never exceed the value for the critical strain ε_{Cr} which is a function of the carbon equivalent value (36) and the Mn/S ratio, as this could cause internal cracks during casting (Hiebler et al, 1994). It should be pointed out that low carbon steels with high Mn/S (>25) ratios are the least prone for cracking during casting.

$$C_{eq,C} = (\%C) + 0.02(\%Mn) + 0.04(\%Ni) - 0.1(\%Si) - 0.04(\%Cr) - 0.1(\%Mo) \tag{36}$$

%Carbon	Temperature range, °C	A_0	m	n	Q_C (kJ/mol)
0.090 (low carbon)	< 1000	0.349	0.35	3.1	150.6
0.090 (low carbon)	1000-1250	2.422	0.33	2.5	146.4
0.090 (low carbon)	> 1250	6.240	0.21	1.6	123.4
0.185 (medium carbon)	< 1000	141.1	0.36	3.1	211.3
0.185 (medium carbon)	1000-1250	1.825	0.37	2.5	144.3
0.185 (medium carbon)	> 1250	1.342	0.25	1.5	102.5

Table 1. Data used for primary creep

3.1.2 Solid fraction analysis

The solid fraction values f_S are very important especially at the final stages of solidification in which soft reduction is applied in many slab casters in an attempt to reduce or minimize any internal segregation problems. The following expressions extracted from the work of (Won et al, 1998) were used:

$$f_S = \left(1 - 2\Omega\kappa\right)^{-1}\left\{1 - \left(\frac{1536 - T}{\sum_j f'\left(C_j\right)}\right)^{\Lambda}\right\} \quad \text{and} \quad \Lambda = \frac{1 - 2\Omega\kappa}{\kappa - 1} \tag{37}$$

$$\sum_j f'\left(C_j\right) = 67.51(\%C) + 9.741(\%Si) + 3.292(\%Mn) + 82.18(\%P) + 155.8(\%S) \tag{38}$$

$$\Omega = \alpha(1 - \exp(-1/\alpha)) - \frac{1}{2}\exp(-1/(2\alpha)) \tag{39}$$

$$\alpha = 33.7 \cdot C_R^{-0.244} \tag{40}$$

$$\kappa = 0.265 \quad \text{and} \quad \kappa = (\kappa^{\delta/L} + \kappa^{\gamma/L}) / 2 \tag{41}$$

As described by equations (37) through (41), considering an average equilibrium partition coefficient κ=0.265 for carbon at the delta/liquid and gamma/liquid phase transformations, respectively, and a local cooling rate C_R, solid fraction values can be computed as a function of mushy-zone temperatures and specific chemical analysis of steel. Dendrites are characterized by means of the primary λ_{PRIM} and secondary λ_{SDAS} dendritic arm spacing. The dependence of both λ_{PRIM} and λ_{SDAS} spacing on the chemical composition and solidification conditions is needed for a correct microstructure prediction whose results can be employed for micro- and macro-segregation appraisal. Primary dendrite arm spacing is related to the solidification rate r and thermal gradient G in the mushy zone according to the following formula (Cabrera-Marrero et al, 1998):

$$\lambda_{PRIM} = n_{rg} \cdot r^{-\frac{1}{4}} \cdot G^{-\frac{1}{2}} \tag{42}$$

Solidification rate r is actually the rate of shell growth:

$$r = \frac{dS}{dt} \tag{43}$$

and the thermal gradient G is defined as:

$$G = \frac{(T_L - T_S)}{w} \tag{44}$$

where w is the width of the mushy zone. It is interesting to note that local solidification times T_F are related to the local cooling rates with the expressions:

$$T_F = \frac{T_L - T_S}{C_R} = \frac{T_L - T_S}{rG} = \frac{T_L - T_S}{G\left(\frac{dS}{dt}\right)} \tag{45}$$

Furthermore, λ_{SDAS} is an important parameter as it plays a great role in the development of micro-segregation towards the final stage of solidification. For this reason it has received more attention than λ_{PRIM}. Consequently, recalling the work of (Won & Thomas, 2001) secondary dendrite arm spacing λ_{SDAS} (in μm) was computed using the following equation:

$$\lambda_{SDAS} = \begin{cases} (169.1 - 720.9 \cdot (\%C)) \cdot C_R^{-0.4935} & \text{for } 0 < (\%C) \le 0.15 \\ 143.9 \cdot C_R^{-0.3616} \cdot (\%C)^{(0.5501 - 1.996 \cdot (\%C))} & \text{for } (\%C) > 0.15 \end{cases} \tag{46}$$

4. Results and discussion

For the Stomana slab caster that normally casts slab sizes of 220x1500 mm x mm two chemical analyses for steel were examined depending on the selected carbon concentrations, as presented on Table 2.

%C	%Si	%Mn	%P	%S	%Cu	%Ni	%Cr	%Al	T_{liq}(°C)	T_{sol}(°C)
0.100	0.30	1.20	0.025	0.015	0.35	0.30	0.10	0.03	1515	1495
0.185	0.30	1.20	0.025	0.015	0.35	0.30	0.10	0.03	1508	1479

Table 2. Steel chemical analyses examined for Stomana

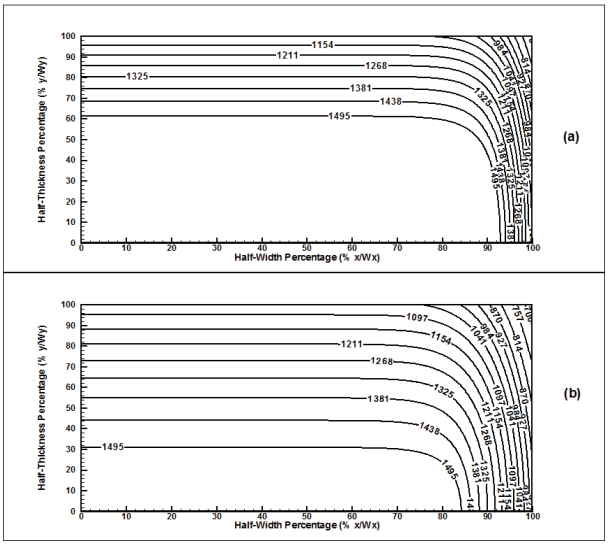

Fig. 1. Temperature distribution in sections of a 220 x 1500 mm x mm Stomana slab, at 5.1 m for part (a) and 10 m for part (b) from the meniscus, respectively. %C = 0.10; casting speed: 0.80 m/min; SPH: 20 K; solidus temperature = 1495°C; *(all temperatures in the graph are in °C)*

In addition to this, two levels for superheat *SPH* (=T_{cast}-T_L) were selected at the values of 20K and 40K. Two levels for the casting speed u_c were also examined at the 0.6 and 0.8 m/min. Fig. 1 presents the temperature distribution till solidus temperature inside a slab at two different positions in the caster; parts (a) and (b) show results at about 5.1 m and 10.0 m from the meniscus level in the mold, respectively. The dramatic progress of the solidification front is illustrated. The following casting parameters were selected in this case: %C=0.10, *SPH*= 20K, and u_c = 0.8 m/min. It is interesting to note that the shell grows faster along the direction of the smaller size, i.e., the thickness than the width of the slab. Fig. 2 presents some more typical results for the same case. The temperature in the centre is presented by line 1, and the temperature at the surface of the slab is presented by line 2. The shell thickness *S* and the distance between liquidus and solidus *w* are presented by dotted lines 3 and 4, respectively. In part (b) of Fig. 2 the rate of shell growth (d*S*/dt), the cooling rate (C_R), and the solid fraction (f_S) in the final stages of solidification are presented. Finally, in part (c) the local solidification time T_F, and secondary dendrite arm spacing λ_{SDAS} are also presented. It is interesting to note that the rate of shell growth is almost constant for the major part of solidification. Computation results show that solid fraction seems to significantly increase towards solidification completion. Apart from unclear fluid-flow phenomena that may adversely affect the uniform development of dendrites in the final stages of solidification

and influence the local solid-fraction values, the shape of the f_S curve at the values of f_S above 0.8 seem to be influenced by the selected set of equations (37)-(41). Fig. 3 depicts computed strain results along the caster.

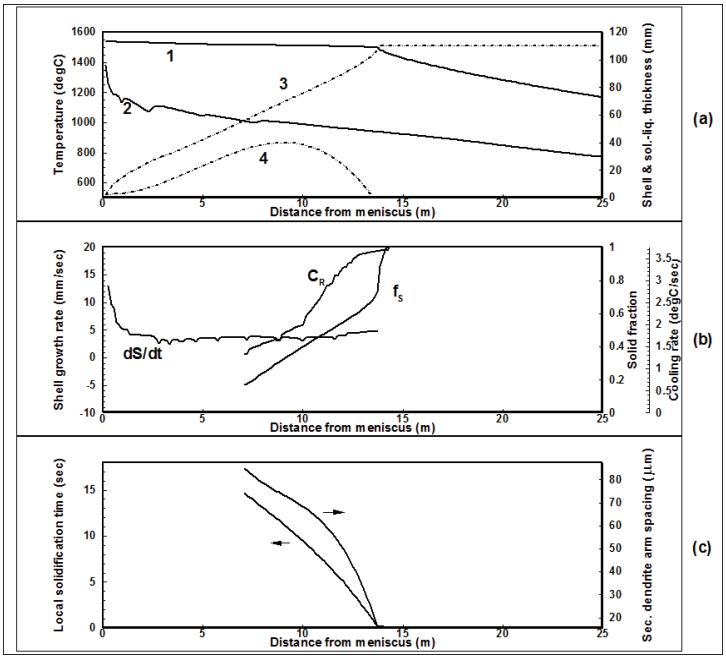

Fig. 2. Results with respect to distance from the meniscus: In part (a), lines (1) and (2) illustrate the centreline and surface temperatures of a 220 x 1500 mm x mm Stomana slab; lines (3) and (4) depict the shell thickness and the distance between the solidus and liquidus temperatures; in part (b), the solid fraction f_S, the local cooling-rate C_R, and the rate of shell growth dS/dt are presented; in part (c), the local solidification time and secondary dendrite arm spacing are depicted, as well. Casting conditions: %C = 0.10; casting speed: 0.80 m/min; SPH: 20 K; solidus temperature = 1495ºC; *(all temperatures in the graph are in ºC)*

In part (a) of Fig. 3 line 1 depicts the bulging strain along the caster with the aforementioned formulation. Left-hand-side (LHS) axis is used to present the bulging strain which is also presented by dashed line 2 with the means of another formulation (Han et al, 2001) which is presented by the following equations:

$$\delta_{B,2} = \frac{\sigma_p \ell_p^{\,4}}{32 E_e S^3} \sqrt{t_p} \tag{47}$$

where most parameters were defined in the appropriate section and E_e is an equivalent elastic modulus that was calculated using the following equation:

$$E_e = \frac{T_S - T_p}{T_S - 100} \times 10^4 \qquad \text{in MPa} \tag{48}$$

Consequently, the bulging strain is computed by equation (20) in which δ_B is substituted by $\delta_{B,2}$. It seems that the computed results in the latter case are much higher than the ones computed with the generally applied method as described in 3.1.1. Furthermore, the recently presented formulation (47)-(48) was proven to be of limited applicability in most cases for the Sovel slab caster and in some cases in the Stomana caster as it gave rise to extremely high values for the bulging strain. Coming back to Fig. 3, the right-hand-side (RHS) axis in part (a) presents the misalignment and unbending strains in a smaller scale. In order to emphasize the misalignment effect upon the strain two different values, 0.5 mm and 1.0 mm of rolls misalignment were chosen at two positions, about 8.9 m and 13.4 m, respectively, along the caster. In this way, these values are depicted by lines 3 and 4 in part (a) of Fig. 3. The caster radius is 10.0 m while two unbending points with radii 18.0 m and 30.0 m at the 13.5 m and 18.0 m positions along the caster were selected in order to simulate the straightening process. Line 8 in part (a) of Fig. 3 actually presents the strain from the first unbending point. The LHS axis in part (b) of Fig. 3 represents the total strains as computed by the two methods for bulging strain and illustrated by lines 5 and 6. In this case, the total strain is less than the critical strain (as measured on the RHS axis and illustrated by straight line 7) throughout the caster.

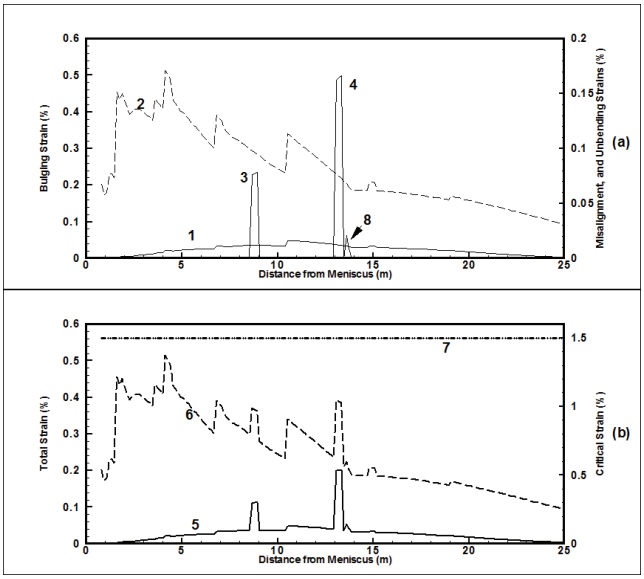

Fig. 3. In part (a), bulging strain (LHS axis), and misalignment and unbending strains (RHS axis) are illustrated. Bulging strain is depicted by two lines (1) and (2) depending on the applied formulation: line (1) is based on the formulation presented in section 3.1.1, and line (2) is based on the formulation described by equations (47) & (48). Lines (3) and (4) depict the strains resulting from 0.5 mm and 1.0 mm rolls-misalignment, respectively. Line (8) shows the strain from unbending at this position of the caster. In a similar manner, the total strains (LHS axis) are presented in part (b); the critical strain (RHS axis) is also, included. Casting conditions: 220 x 1500 mm x mm Stomana slab;%C = 0.10; casting speed: 0.80 m/min; SPH: 20 K; solidus temperature = 1495°C

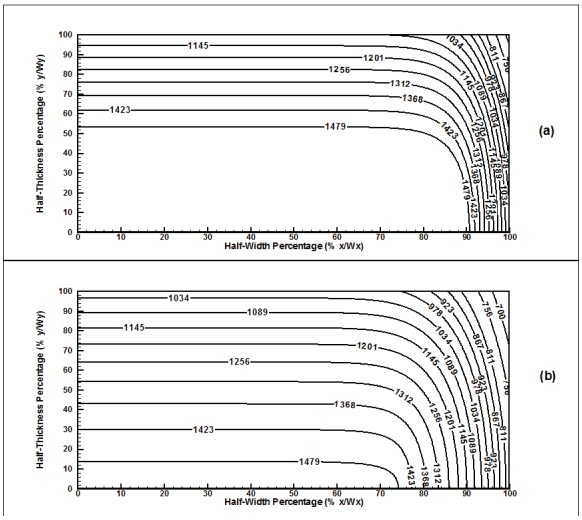

Fig. 4. Temperature distribution in sections of a 220 x 1500 mm x mm Stomana slab, at 8.0 m for part (a) and 16 m for part (b) from the meniscus, respectively. %C = 0.185; casting speed: 0.80 m/min; SPH: 20 K; solidus temperature = 1479ºC; *(all temperatures in the graph are in ºC)*

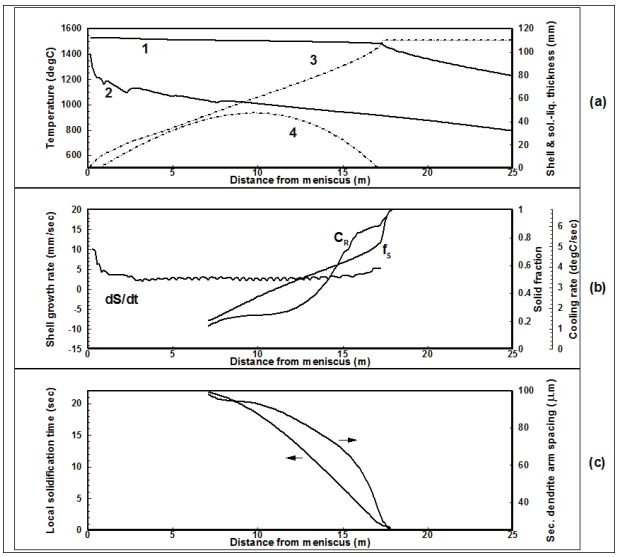

Fig. 5. Results with respect to distance from the meniscus: In part (a), lines (1) and (2) illustrate the centreline and surface temperatures of a 220 x 1500 mm x mm Stomana slab; lines (3) and (4) depict the shell thickness and the distance between the solidus and liquidus temperatures; in part (b), the solid fraction f_S, the local cooling-rate C_R, and the rate of shell growth dS/dt are presented; in part (c), the local solidification time and secondary dendrite arm spacing are depicted, as well. Casting conditions: %C = 0.185; casting speed: 0.80 m/min; SPH: 20 K; solidus temperature = 1479ºC; *(all temperatures in the graph are in ºC)*

Fig. 4 presents the temperature distribution till solidus temperature inside a slab at two different positions in the caster; parts (a) and (b) show results at about 8.0 m and 16.0 m from the meniscus level in the mold, respectively. The following casting parameters were selected in this case: %C=0.185, *SPH*= 20K, and u_c = 0.8 m/min. It is interesting to note that the shell grows faster along the direction of the smaller size, i.e., the thickness than the width of the slab. Fig. 5 presents some more typical results for the same case. The temperature in the centre is presented by line 1, and the temperature at the surface of the slab is presented by line 2. The shell thickness S and the distance between liquidus and solidus w are presented by dotted lines 3 and 4, respectively. In part (b) of Fig. 2 the rate of shell growth (dS/dt), the cooling rate (C_R), and the solid fraction (f_S) in the final stages of solidification are presented. Finally, in part (c) the local solidification time T_F, and secondary dendrite arm spacing λ_{SDAS} are also presented. It is interesting to note that the rate of shell growth is almost constant for the major part of solidification.

In part (a) of Fig. 6 line 1 depicts the bulging strain along the caster with the aforementioned formulation. LHS axis is used to present the bulging strain, while the RHS axis in part (a) presents the misalignment and unbending strains in a smaller scale. The strains due to the applied misalignment values are depicted by lines 2 and 3 in part (a) of Fig. 6. Line 4 presents the strain from the first unbending point. The LHS axis in part (b) of Fig. 6 represents the total strain and is illustrated by line 5. In this case, the total strain is less than the critical strain (as measured on the RHS axis and illustrated by straight line 6) throughout the caster.

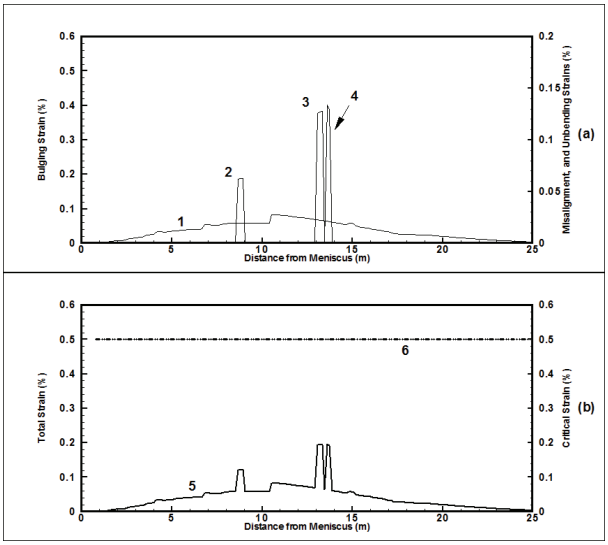

Fig. 6. In part (a), bulging strain (LHS axis), and misalignment and unbending strains (RHS axis) are illustrated. Bulging strain is depicted by line (1); lines (2) and (3) depict the strains resulting from 0.5 mm and 1.0 mm rolls-misalignment, respectively; line (4) shows the strain from unbending at this position of the caster. In a similar manner, the total strain (LHS axis) is presented in part (b); the critical strain (RHS axis) is also, included. Casting conditions: 220 x 1500 mm x mm Stomana slab; %C = 0.185; casting speed: 0.80 m/min; SPH: 20 K; solidus temperature = 1479°C

Fig. 7 presents the temperature distribution till solidus temperature inside a slab at two different positions in the caster; parts (a) and (b) show results at about 9.3 m and 20.0 m from the meniscus level in the mold, respectively. The following casting parameters were selected in this case: %C=0.185, *SPH*=40K, and u_c = 0.8 m/min. It is interesting to note that the shell grows faster along the direction of the smaller size, i.e., the thickness than the width of the slab. Fig. 8 presents some more typical results for the same case. The temperature in the centre is presented by line 1, and the temperature at the surface of the slab is presented by line 2. The shell thickness S and the distance between liquidus and solidus w are presented by dotted lines 3 and 4, respectively. In part (b) of Fig. 2 the rate of shell growth (dS/dt), the cooling rate (C_R), and the solid fraction (f_S) in the final stages of solidification are presented. Finally, in part (c) the local solidification time T_F, and secondary dendrite arm spacing λ_{SDAS} are also presented. It is interesting to note that the rate of shell growth is almost constant for the major part of solidification.

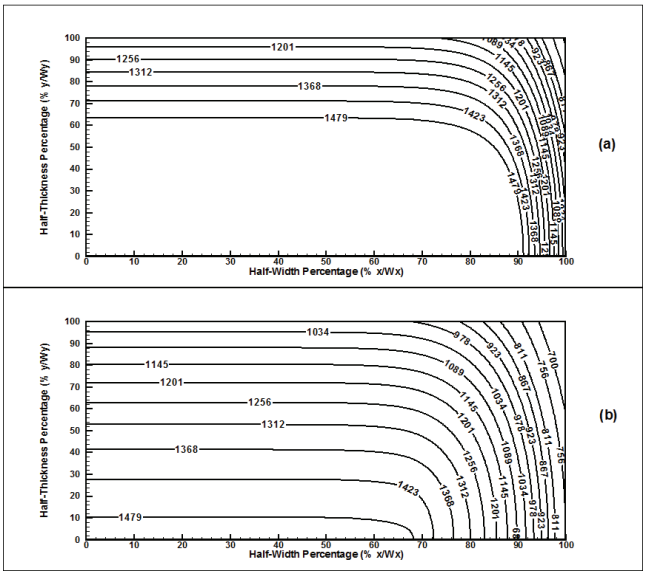

Fig. 7. Temperature distribution in sections of a 220 x 1500 mm x mm Stomana slab, at 9.3 m for part (a) and 20 m for part (b) from the meniscus, respectively. %C = 0.185; casting speed: 0.80 m/min; SPH: 40 K; solidus temperature = 1479°C; *(all temperatures in the graph are in °C)*

In part (a) of Fig. 9 line 1 depicts the bulging strain along the caster with the aforementioned formulation. LHS axis is used to present the bulging strain, while the RHS axis in part (a) presents the misalignment and unbending strains in a smaller scale. The strains due to the applied misalignment values are depicted by lines 2 and 3 in part (a) of Fig. 9. Line 4 presents the strain from the first unbending point, while line 5 presents the strain from the second unbending point. The LHS axis in part (b) of Fig. 9 represents the total strain and is illustrated by line 6. In this case, the total strain is less than the critical strain (as measured on the RHS axis and illustrated by straight line 7) throughout the caster.

For the Sovel slab caster that normally casts slab sizes of 130x390 and 130x360 (mm x mm) two chemical analyses for steel were examined depending on the selected carbon

concentrations, as presented on Table 3. For the cases presented in this study only the slab size of 130x390 was examined.

%C	%Si	%Mn	%P	%S	%Cu	%Ni	%Cr	%V	%Al	T_{liq}(°C)	T_{sol}(°C)
0.100	0.25	1.20	0.025	0.010	0.28	0.30	0.10	0.05	0.04	1516	1497
0.165	0.25	1.20	0.025	0.010	0.28	0.30	0.10	0.05	0.04	1511	1484

Table 3. Steel chemical analyses examined for Sovel

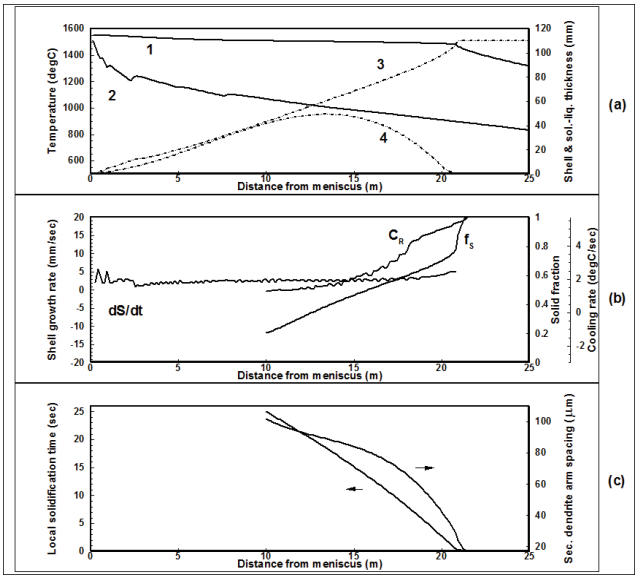

Fig. 8. Results with respect to distance from the meniscus: In part (a), lines (1) and (2) illustrate the centreline and surface temperatures of a 220 x 1500 mm x mm Stomana slab; lines (3) and (4) depict the shell thickness and the distance between the solidus and liquidus temperatures; in part (b), the solid fraction f_S, the local cooling-rate C_R, and the rate of shell growth dS/dt are presented; in part (c), the local solidification time and secondary dendrite arm spacing are depicted, as well. Casting conditions: %C = 0.185; casting speed: 0.80 m/min; SPH: 40 K; solidus temperature = 1479°C; *(all temperatures in the graph are in °C)*

Fig. 10 presents the temperature distribution till solidus temperature inside a slab at two different positions in the caster; parts (a) and (b) show results at about 3.3 m and 6.0 m from the meniscus level in the mold, respectively. The following casting parameters were selected in this case: %C=0.10, *SPH*= 20K, and u_c = 1.1 m/min. It is interesting to note that the shell grows faster along the direction of the smaller size, i.e., the thickness than the width of the slab. Fig. 11 presents some more typical results for the same case. The temperature in the centre is presented by line 1, and the temperature at the surface of the slab is presented by line 2. The shell thickness S and the distance between liquidus and solidus w are presented by dotted lines 3 and 4, respectively. In part (b) of Fig. 11 the rate of shell growth (dS/dt), the cooling rate (C_R), and the solid fraction (f_S) in the final stages of solidification are

presented. Finally, in part (c) the local solidification time T_F, and secondary dendrite arm spacing λ_{SDAS} are also presented. It is interesting to note that the rate of shell growth is almost constant for the major part of solidification.

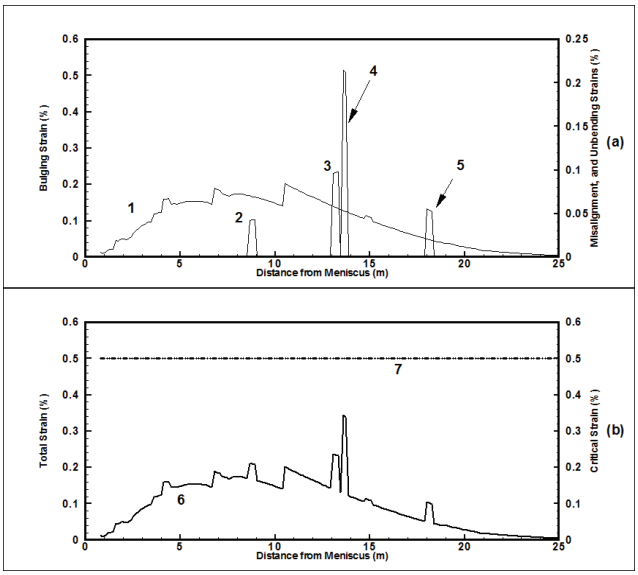

Fig. 9. In part (a), bulging strain (LHS axis), and misalignment and unbending strains (RHS axis) are illustrated. Bulging strain is depicted by line (1); lines (2) and (3) depict the strains resulting from 0.5 mm and 1.0 mm rolls-misalignment, respectively; lines (4) and (5) show the strain from unbending at these positions. In a similar manner, the total strain (LHS axis) is presented in part (b) as line (6); the critical strain (RHS axis) is also included as line (7). Casting conditions: 220 x 1500 mm x mm Stomana slab; %C = 0.185; casting speed: 0.80 m/min; SPH: 40 K; solidus temperature = 1479^{o}C

In part (a) of Fig. 12 line 1 depicts the bulging strain along the caster with the aforementioned formulation. LHS axis is used to present the bulging strain, while the RHS axis in part (a) presents the misalignment and unbending strains in a larger scale. The caster radius is 9.0 m and unbending takes place at a point about 13.5 m apart from meniscus level with a straightening radius of about 16.0 m. It seems that the computed unbending strains are relatively low. Due to the small size of the produced slabs the design of the caster has a relatively small number of rolls at large distances from each other. Roll pitches have values from 2.5 m up to 3.0 m. In this way the caster is somewhat "forgiving" in the cases that misalignment gets a bit out of hand. Actually, in this study relatively large misalignment values from 20 mm up to 50 mm were examined. The strains due to the applied misalignment values are depicted by line 2 in part (a) of Fig. 12, and seem to be low indeed. For the Sovel caster, bulging strains were computed by the formulation presented in section 3.1.1; too high values for bulging strains were computed with the formulation presented by equations (47) and (48). The LHS axis in part (b) of Fig. 12 represents the total strain and is illustrated by line 3. In this case, the total strain is less than the critical strain (as measured on the RHS axis and illustrated by straight line 4) throughout the caster.

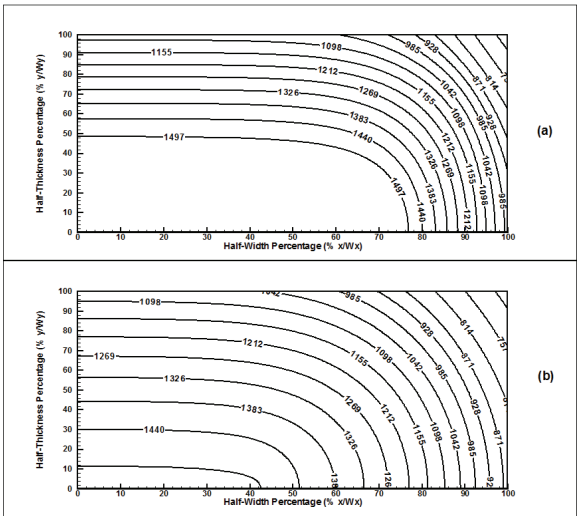

Fig. 10. Temperature distribution in sections of a 130 x 390 mm x mm Sovel slab, at 3.3 m for part (a) and 6.0 m for part (b) from the meniscus, respectively. %C = 0.10; casting speed: 1.1 m/min; *SPH*: 20 K; solidus temperature = 1497ºC; *(all temperatures in the graph are in ºC)*

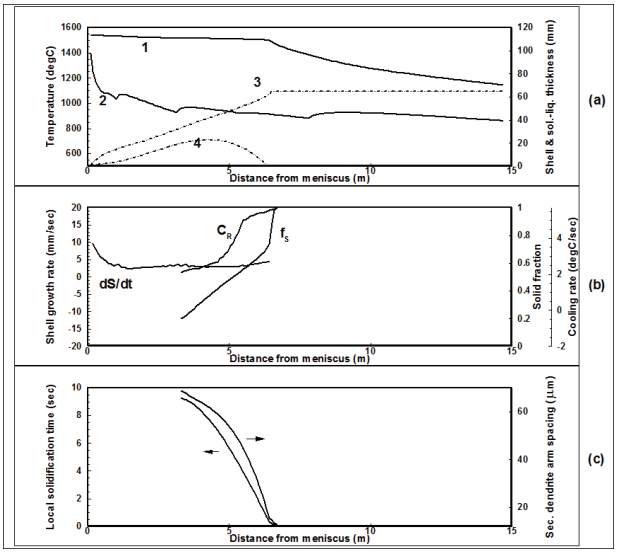

Fig. 11. Results with respect to distance from the meniscus: In part (a), lines (1) and (2) illustrate the centreline and surface temperatures of a 130 x 390 mm x mm Sovel slab; lines (3) and (4) depict the shell thickness and the distance between the solidus and liquidus temperatures; in part (b), the solid fraction f_S, the local cooling-rate C_R, and the rate of shell growth dS/dt are presented; in part (c), the local solidification time and secondary dendrite arm spacing are depicted, as well. Casting conditions: %C = 0.10; casting speed: 1.1 m/min; SPH: 20 K; solidus temperature = 1497ºC; *(all temperatures in the graph are in ºC)*

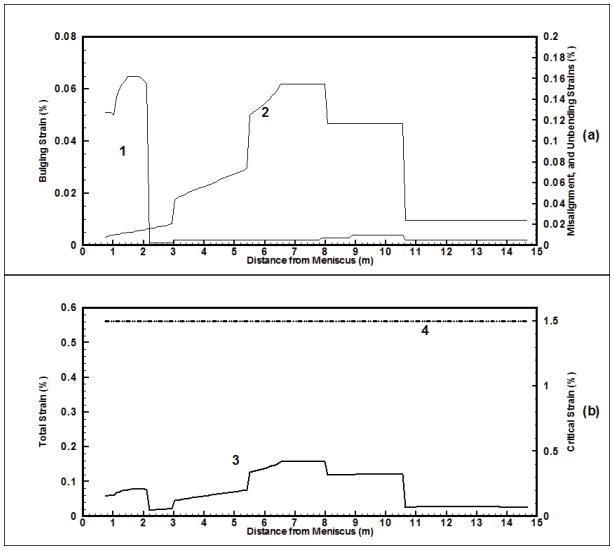

Fig. 12. In part (a), bulging strain (LHS axis), and misalignment and unbending strains (RHS axis) are illustrated by lines (1) and (2), respectively. In a similar manner, the total strain (LHS axis) is presented in part (b) as line (3); the critical strain (RHS axis) is also included as line (4). Casting conditions: 130 x 390 mm x mm Sovel slab; %C = 0.10; casting speed: 1.1 m/min; SPH: 20 K; solidus temperature = 1497°C

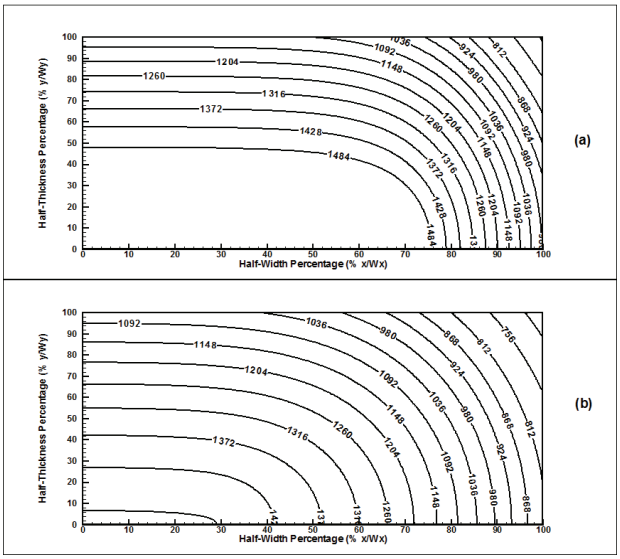

Fig. 13. Temperature distribution in sections of a 130 x 390 mm x mm Sovel slab, at 4.0 m for part (a) and 7.7 m for part (b) from the meniscus, respectively. %C = 0.165; casting speed: 1.1 m/min; *SPH*: 20 K; solidus temperature = 1484°C; *(all temperatures in the graph are in °C)*

Fig. 13 presents the temperature distribution till solidus temperature inside a slab at two different positions in the caster; parts (a) and (b) show results at about 4.0 m and 7.7 m from the meniscus level in the mold, respectively. The following casting parameters were selected in this case: %C=0.165, *SPH*= 20K, and u_c = 1.1 m/min. It is interesting to note that the shell grows faster along the direction of the smaller size, i.e., the thickness than the width of the slab. Fig. 14 presents some more typical results for the same case. The temperature in the centre is presented by line 1, and the temperature at the surface of the slab is presented by line 2. The shell thickness S and the distance between liquidus and solidus w are presented by dotted lines 3 and 4, respectively. In part (b) of Fig. 14 the rate of shell growth (dS/dt), the cooling rate (C_R), and the solid fraction (f_S) in the final stages of solidification are presented. Finally, in part (c) the local solidification time T_F, and secondary dendrite arm spacing λ_{SDAS} are also presented. It is interesting to note that the rate of shell growth is almost constant for the major part of solidification.

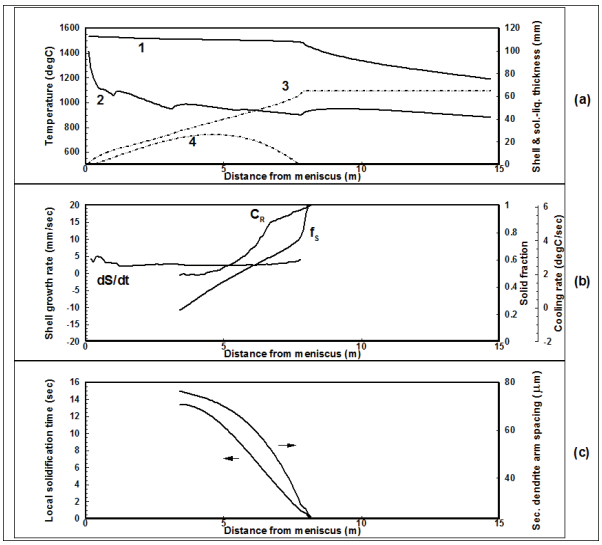

Fig. 14. Results with respect to distance from the meniscus: In part (a), lines (1) and (2) illustrate the centreline and surface temperatures of a 130 x 390 mm x mm Sovel slab; lines (3) and (4) depict the shell thickness and the distance between the solidus and liquidus temperatures; in part (b), the solid fraction f_S, the local cooling-rate C_R, and the rate of shell growth dS/dt are presented; in part (c), the local solidification time and secondary dendrite arm spacing are depicted, as well. Casting conditions: %C = 0.165; casting speed: 1.1 m/min; SPH: 20 K; solidus temperature = 1484ºC; *(all temperatures in the graph are in ºC)*

In part (a) of Fig. 15, line 1 depicts the bulging strain along the caster with the aforementioned formulation. LHS axis is used to present the bulging strain, while the RHS axis in part (a) presents the misalignment and unbending strains in the same scale. The strains due to the applied misalignment values are depicted by line 2 in part (a) of Fig. 15, and seem to be low indeed. The LHS axis in part (b) of Fig. 15 represents the total strain and is illustrated by line 3. In this case, the total strain is less than the critical strain (as measured on the RHS axis and illustrated by straight line 4) throughout the caster.

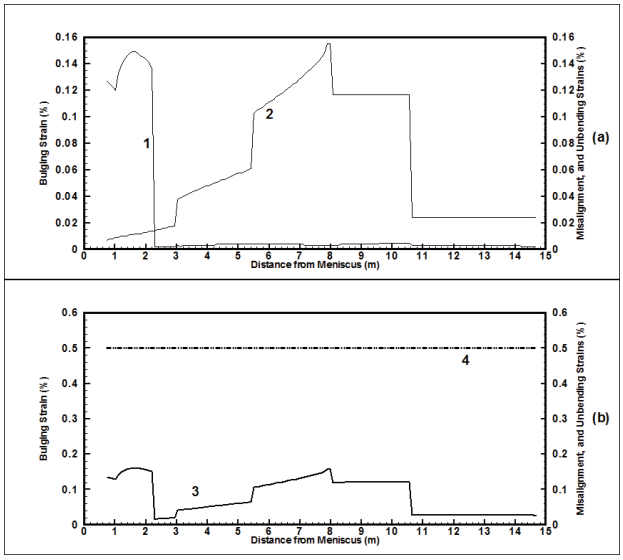

Fig. 15. In part (a), bulging strain (LHS axis), and misalignment and unbending strains (RHS axis) are illustrated by lines (1) and (2), respectively. In a similar manner, the total strain (LHS axis) is presented in part (b) as line (3); the critical strain (RHS axis) is also included as line (4). Casting conditions: 130 x 390 mm x mm Sovel slab; %C = 0.165; casting speed: 1.1 m/min; SPH: 20 K; solidus temperature = 1484ºC

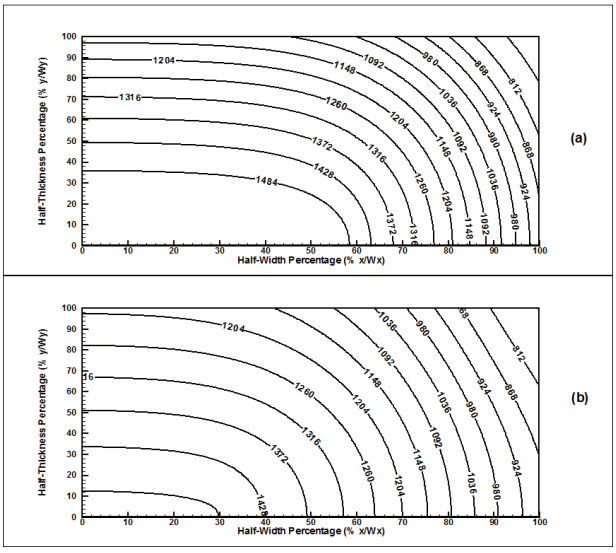

Fig. 16. Temperature distribution in sections of a 130 x 390 mm x mm Sovel slab, at 7.3 m for part (a) and 9.5 m for part (b) from the meniscus, respectively. %C = 0.165; casting speed: 1.1 m/min; *SPH*: 40 K; solidus temperature = 1484ºC; *(all temperatures in the graph are in ºC)*

Fig. 16 presents the temperature distribution till solidus temperature inside a slab at two different positions in the caster; parts (a) and (b) show results at about 7.3 m and 9.5 m from the meniscus level in the mold, respectively. The following casting parameters were selected in this case: %C=0.165, *SPH*= 40K, and u_c = 1.1 m/min. It is interesting to note that the shell grows faster along the direction of the smaller size, i.e., the thickness than the width of the slab. Fig. 17 presents some more typical results for the same case. The temperature in the centre is presented by line 1, and the temperature at the surface of the slab is presented by line 2. The shell thickness *S* and the distance between liquidus and solidus *w* are presented by dotted lines 3 and 4, respectively. In part (b) of Fig. 17 the rate of shell growth (d*S*/dt), the cooling rate (C_R), and the solid fraction (f_S) in the final stages of solidification are presented. Finally, in part (c) the local solidification time T_F, and secondary dendrite arm spacing λ_{SDAS} are also presented. It is interesting to note that the rate of shell growth is almost constant for the major part of solidification.

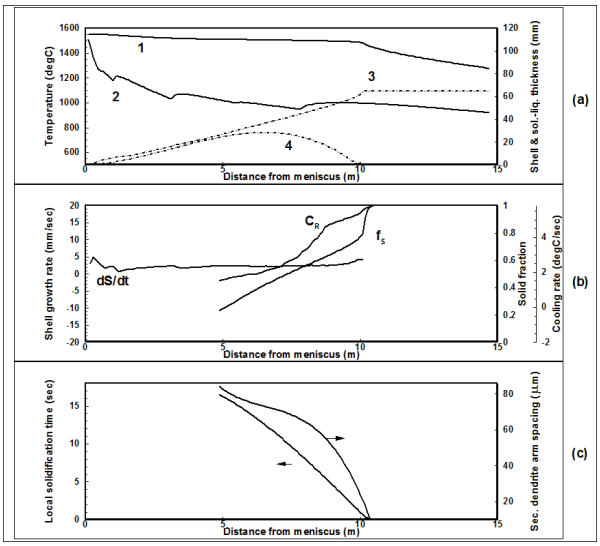

Fig. 17. Results with respect to distance from the meniscus: In part (a), lines (1) and (2) illustrate the centreline and surface temperatures of a 130 x 390 mm x mm Sovel slab; lines (3) and (4) depict the shell thickness and the distance between the solidus and liquidus temperatures; in part (b), the solid fraction f_S, the local cooling-rate C_R, and the rate of shell growth d*S*/dt are presented; in part (c), the local solidification time and secondary dendrite arm spacing are depicted, as well. Casting conditions: %C = 0.165; casting speed: 1.1 m/min; SPH: 40 K; solidus temperature = 1484ºC; *(all temperatures in the graph are in ºC)*

In part (a) of Fig. 18 line 1 depicts the bulging strain along the caster with the aforementioned formulation. LHS axis is used to present the bulging strain, while the RHS axis in part (a) presents the misalignment and unbending strains in the same scale. The strains due to the applied misalignment values are depicted by line 2 in part (a) of Fig. 18, and seem to be low indeed. The LHS axis in part (b) of Fig. 18 represents the total strain and is illustrated by line 3. However in this case, the total strain is larger than the critical strain (as measured on the RHS axis and illustrated by straight line 4) in as far as the first 4 m of

the caster are concerned. The effect of high SPH is affecting the internal slab soundness in a negative way.

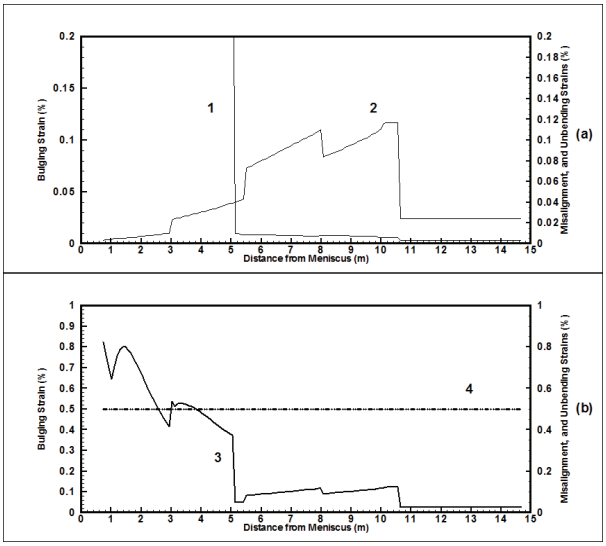

Fig. 18. In part (a), bulging strain (LHS axis), and misalignment and unbending strains (RHS axis) are illustrated by lines (1) and (2), respectively. In a similar manner, the total strain (LHS axis) is presented in part (b) as line (3); the critical strain (RHS axis) is also included as line (4). Casting conditions: 130 x 390 mm x mm Sovel slab; %C = 0.165; casting speed: 1.1 m/min; SPH: 40 K; solidus temperature = 1484^{o}C

As of figures 1, 4, 7, 10, 13, and 16 it is obvious that the temperature distribution is presented only for the one-quarter of the slab cross-section, the rest one is omitted as redundant due to symmetry. It is interesting to note that due to the values of the shape factors, i.e., 1500/220 = 6.818, and 390/130 = 3.0 for the Stomana and Sovel casters, respectively, the shell proceeds faster across the largest size (width) than across the smallest one (thickness). This is well depicted with respect to the plot of the temperature distributions in the sections till the solidus temperatures for the specific chemical analyses under study. It should be pointed out that due to this, macro-segregation phenomena occasionally appear at both ends and across the central region of slabs. These defects appear normally as edge defects later on at the plate mill once they are rolled.

Comparing figures 2 and 5, it becomes evident that the higher the carbon content the more it takes to solidify downstream the Stomana caster. For the Sovel caster similar results can be obtained by comparing the graphs presented by figures 11 and 14.

Comparing figures 5 and 8, it is interesting to note that the higher the superheat the more time it takes for a slab to completely solidify in the caster at Stomana. Similar results have been obtained for the Sovel caster, just by comparing the results presented in figures 14 and 17.

Furthermore, the higher the casting speed the more it takes to complete solidification in both casters, although computed results are not presented at different casting speeds. For productivity reasons, the maximum attainable casting speeds are selected in normal

practice, so to avoid redundancy only results at real practice casting speeds were selected for presentation in this study.

The ratio of the shape factors for the two casters, i.e., 6.818/3.0 = 2.27 seems to play some role for the failure of the application of the second formulation presented by equations (47) and (48) for the Sovel caster compared with the formulation for the bulging calculations presented in 3.1.1. In addition to this, even for the Stomana caster the computed bulging results were too high and not presented at higher carbon and superheat values. Low carbon steel grades seem to withstand better any bulging, misalignment, and unbending strains for both casters as illustrated by figures 3 and 6 for Stomana, and figures 12 and 15 for Sovel, respectively. The higher critical strain values associated with low carbon steels give more "room" for higher superheats and any caster design or maintenance problems.

Another critical aspect that is worth mentioning is the effect of SPH upon strains for the same steel grade and casting speed. For the Stomana caster, comparing the results presented in figures 6 and 9 it seems that by increasing the superheat from 20K to 40K the bulging and misalignment strains increase by an almost double value; furthermore, the unbending strain at the second straightening point becomes appreciable and apparent in figure 9. In the case of the Sovel caster, higher superheat gives rise to such high values for bulging strains that may create significant amount of internal defects in the first stages of solidification, as presented in Fig. 18 compared with Fig. 15. Consequently, although Sovel's caster is more "forgiving" than Stomana's one with respect to unbending and misalignment strains it gets more prone to create defects due to bulging strains at higher superheats.

In Fig. 19, an attempt to model static soft reduction is presented for the Stomana caster. In fact, statistical analysis was performed based upon the overall computed results and the following equation was developed from regression analysis giving the solidification point (SP) in meters, that is, the distance from meniscus at which the slab is completely solidified:

$$SP = 0.16 \times SPH + 37.5 \times \%C + 19.7 \times u_C - 8.5 \tag{49}$$

Equation (49) is statistically sound with a correlation coefficient R^2=0.993, an F-test for the regression above 99.5%, and t-test for every coefficient above 99.5%, as well. In general, industrial practice has revealed that in the range of solid fraction from 0.3 up to 0.7 is the most fruitful time to start applying soft reduction. In the final stages of solidification, internal segregation problems may appear. In the Stomana caster, the final and most critical segments are presented in Fig. 19 with the numbers 5, 6, and 7. A scheme for static soft reduction (SR) is proposed with the idea of closing the gaps of the rolls according to a specific profile. In this way, the reduction of the thickness of the final product per caster length in which static soft reduction is to be applied will be of the order of 0.7 mm/m, which is similar to generally applied practices of the order of 1.0 mm/m. At the same time, for the conditions presented in Fig. 19, the solid fraction will be around 0.5 at the time soft reduction starts. Consequently, the point within the caster at which static soft reduction can be applied (starting $f_S \approx 0.5$) is given by:

$$SR_{start} \simeq SP - 5.5 \tag{50}$$

where, SR_{start} designates the caster point in meters at which static soft reduction may prove very promising.

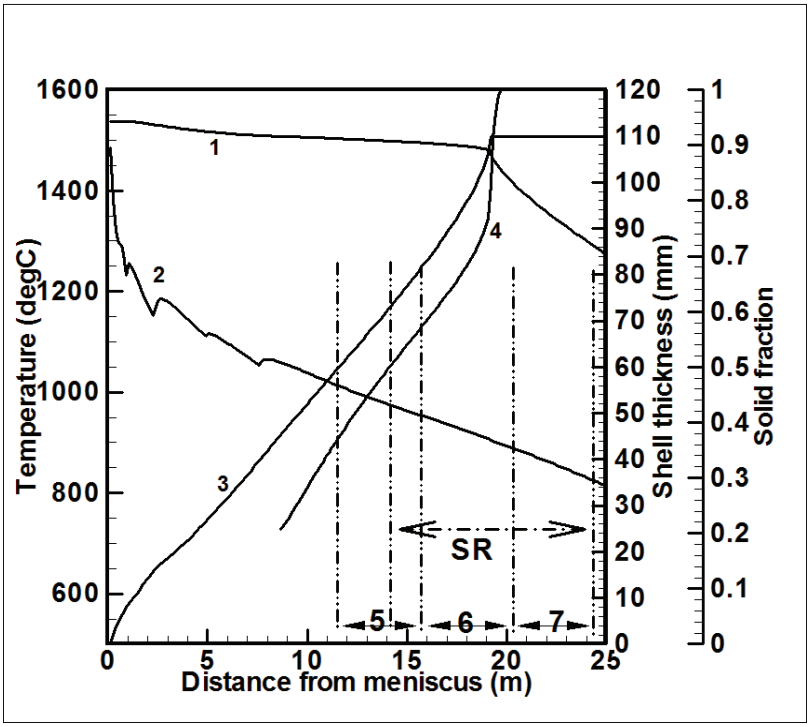

Fig. 19. Suggested area for static soft reduction (SR) in the Stomana caster: Casting conditions: 220x1500 mm x mm slab; %C = 0.185; *SPH* = 30 K; u_C = 0.8 m/min. Lines 1 and 2 depict the centreline and surface temperature, respectively. Lines 3 and 4 illustrate the shell growth and solid fraction, respectively. The borders of the final casting segments 5, 6, and 7 are also presented

Closing the discussion it should be added that the proper combination of low superheat and high casting speed values satisfies a proper slab unbending in the caster. The straightening process is successfully carried out at slab temperatures above 900°C without any surface defects for the products.

5. Conclusion

In this computational study the differential equation of heat transfer was numerically solved along a continuous caster, and results that are interesting from both the heat-transfer and the metallurgical points of view were presented and discussed. The effects of superheat, casting speed, and carbon levels upon slab casting were examined and computed for Stomana and Sovel casters. Generally, the higher the superheat the more difficult to solidify and produce a slab product that will be free of internal defects. Carbon levels are related to the selected steel grades, and casting speeds to the required maximum productivities so both are more difficult to alter under normal conditions. In order to tackle any internal defects coming from variable superheats from one heat to another, dynamic soft reduction has been put into practice by some slab casting manufacturers worldwide. In this study,

some ideas for applying static soft reduction in practice at the Stomana caster have been proposed; in this case, more stringent demands for superheat levels from one heat to another are inevitable.

6. Acknowledgment

The continuous support from the top management of the SIDENOR group of companies is greatly appreciated. Professor Rabi Baliga from McGill University, Montreal, is also acknowledged for his guidelines in the analysis of many practical computational heat-transfer problems. The help of colleague and friend, mechanical engineer Nicolas Evangeliou for the construction of the graphs is also greatly appreciated.

7. References

Brimacombe J.K. (1976). Design of Continuous Casting Machines based on a Heat-Flow Analysis : State-of-the-Art Review. *Canadian Metallurgical Quarterly, CIM,* Vol. 15, No. 2, pp. 163-175

Brimacombe J.K., Sorimachi K. (1977). Crack Formation in the Continuous Casting of Steel. *Met. Trans.B,* Vol. 8B, pp. 489-505

Brimacombe J.K., Samarasekera I.V. (1978). The Continuous-Casting Mould. *Intl. Metals Review,* Vol. 23,No. 6, pp. 286-300

Brimacombe J.K., Samarasekera (1979). The Thermal Field in Continuous Casting Moulds. *CanadianMetallurgical Quarterly, CIM,* Vol. 18, pp. 251-266

Brimacombe J.K., Weinberg F., Hawbolt E.B. (1979). Formation of Longitudinal, Midface Cracks inContinuously Cast Slabs. *Met. Trans. B,* Vol. 10B, pp. 279-292

Brimacombe J.K., Hawbolt E.B., Weinberg F. (1980). Formation of Off-Corner Internal Cracks inContinuously-Cast Billets, *Canadian Metallurgical Quarterly, CIM,* Vol. 19, pp. 215-227

Burmeister L.C. (1983). Convective Heat Transfer. *John Wiley & Sons,* p. 551

Cabrera-Marrero, J.M., Carreno-Galindo V., Morales R.D., Chavez-Alcala F. (1998). Macro-Micro Modeling of the Dendritic Microstructure of Steel Billets by Continuous Casting. *ISIJ International,* Vol. 38, No. 8, pp. 812-821

Carslaw, H.S, & Jaeger, J.C. (1986). Conduction of Heat in Solids. *Oxford University Press.* New York

Churchill, S.W., & Chu, H.H.S. (1975). Correlating Equations for Laminar and Turbulent Free Convection from a Horizontal Cylinder. *Int. J. Heat Mass Transfer,* 18, pp. 1049-1053

Fujii, H., Ohashi, T., & Hiromoto, T. (1976). On the Formation of Internal Cracks in Continuously Cast Slabs. *Tetsu To Hagane-Journal of the Iron and Steel Institute of Japan,* Vol. 62, pp. 1813-1822

Fujii, H., Ohashi, T., Oda, M., Arima, R., & Hiromoto, T. (1981). Analysis of Bulging in Continuously Cast Slabs by the Creep Model. *Tetsu To Hagane-Journal of the Iron and Steel Institute of Japan,* Vol. 67, pp. 1172-1179

Grill A., Schwerdtfeger K. (1979). Finite-element analysis of bulging produced by creep in continuously cast steel slabs. *Ironmaking and Steelmaking,* Vol. 6, No. 3, pp. 131-135

Han, Z., Cai, K., & Liu, B. (2001). Prediction and Analysis on Formation of Internal Cracks in Continuously Cast Slabs by Mathematical Models. *ISIJ International,* Vol. 41, No. 12, pp. 1473-1480

Hiebler, H., Zirngast, J., Bernhard, C., & Wolf, M. (1994). Inner Crack Formation in Continuous Casting: Stress or Strain Criterion? *Steelmaking Conference Proceedings,* ISS, Vol. 77, pp. 405-416

Imagumbai, M. (1994). Relationship between Primary- and Secondary-dendrite Arm Spacing of C-Mn Steel Uni-directionally Solidified in Steady State. *ISIJ International,* Vol. 34, No. 12, pp. 986-991

Incropera, F.P., & DeWitt, D.P. (1981). Fundamentals of Heat Transfer. *John Wiley & Sons*, p. 49

Kozlowski, P.F., Thomas, B.G., Azzi, J.A., & Wang, H. (1992). Simple Constitutive Equations for Steel at High Temperature. *Metallurgical Transactions A,* Vol. 23A, (March 1992), pp. 903-918

Lait, J.E., Brimacombe, J.K., Weinberg, F. (1974). Mathematical Modelling of Heat Flow in the Continuous Casting of Steel. *Ironmaking and Steelmaking,* Vol. 1, No.2, pp. 90-97

Ma, J., Xie, Z., & Jia G. (2008). Applying of Real-time Heat Transfer and Solidification Model on the Dynamic Control System of Billet Continuous Casting. *ISIJ International,* Vol. 48, No. 12, pp. 1722-1727

Matsumiya, T., Kajioka, H., Mizoguchi, S., Ueshima, Y., & Esaka, H. (1984). Mathematical Analysis of Segregations in Continuously-cast Slabs. *Transactions ISIJ,* Vol. 24, pp. 873-882

Mizikar, E.A. (1967). Mathematical Heat Transfer Model for Solidification of Continuously Cast Steel

Slabs. *Trans. TMS-AIME,* Vol. 239, pp. 1747-1753

Palmaers, A. (1978). High Temperature Mechanical Properties of Steel as a Means for Controlling Casting. *Metall. Report C.R.M.,* No. 53, pp. 23-31

Patankar, S.V. (1980). Numerical Heat Transfer and Fluid Flow. *Hemisphere Publishing Corporation,* Washington

Pierer, R., Bernhard, C., & Chimani, C. (2005). Evaluation of Common Constitutive Equations for Solidifying Steel. *BHM,* Vol. 150, No. 5, pp. 1-13

Sismanis P.G. (2010). Heat transfer analysis of special reinforced NSC-columns under severe fire conditions. *International Journal of Materials Research (formerly: Zeitschrift fuer Metallkunde),* Vol. 101, (March 2010), pp. 417-430, DOI 10.3139/146.110290

Sivaramakrishnan S., Bai H., Thomas B.G., Vanka P., Dauby P., & Assar M. (2000). *Ironmaking Conference Proceedings,* Pittsburgh, PA, ISS, Vol. 59, pp. 541-557

Tacke K.-H. (1985). Multi-beam model for strand straightening in continuous caster. *Ironmaking and Steelmaking,* Vol. 12, No. 2, pp. 87-94

Thomas, B.G., Samarasekera, I.V., Brimacombe, J.K. (1987). Mathematical Model of the Thermal Processing of Steel Ingots: Part I. Heat Flow Model. *Metallurgical Transactions B,* Vol. 18B, (March 1987), pp. 119-130

Uehara, M., Samarasekera, I.V., Brimacombe, J.K. (1986). Mathematical modeling of unbending of continuously cast steel slabs. *Ironmaking and Steelmaking.* Vol. 13, No. 3, pp. 138-153

Won, Y-M, Kim, K-H, Yeo, T-J, & Oh, K. (1998). Effect of Cooling Rate on ZST, LIT and ZDT of Carbon Steels Near Melting Point. *ISIJ International,* Vol. 38, No. 10, pp. 1093-1099

Won, Y-M, & Thomas, B. (2001). Simple Model of Microsegregation during Solidification of Steels. *Metallurgical and Materials Transactions A,* Vol. 32A, (July 2001), pp. 1755-1767

Yoon, U-S., Bang, I.-W., Rhee, J.H., Kim, S.-Y., Lee, J.-D., & Oh, K.-H. (2002). Analysis of Mold Level Hunching by Unsteady Bulging during Thin Slab Casting. *ISIJ International,* Vol. 42, No. 10, pp. 1103-1111

Zhu, G., Wang, X., Yu, H., & Wang, W. (2003). Strain in solidifying shell of continuous casting slabs. *Journal of University of Science and Technology Beijing,* Vol. 10, No. 6, pp. 26-29

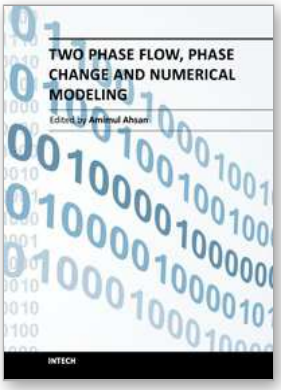

Two Phase Flow, Phase Change and Numerical Modeling

Edited by Dr. Amimul Ahsan

ISBN 978-953-307-584-6
Hard cover, 584 pages
Publisher InTech
Published online 26, September, 2011
Published in print edition September, 2011

The heat transfer and analysis on laser beam, evaporator coils, shell-and-tube condenser, two phase flow, nanofluids, complex fluids, and on phase change are significant issues in a design of wide range of industrial processes and devices. This book includes 25 advanced and revised contributions, and it covers mainly (1) numerical modeling of heat transfer, (2) two phase flow, (3) nanofluids, and (4) phase change. The first section introduces numerical modeling of heat transfer on particles in binary gas-solid fluidization bed, solidification phenomena, thermal approaches to laser damage, and temperature and velocity distribution. The second section covers density wave instability phenomena, gas and spray-water quenching, spray cooling, wettability effect, liquid film thickness, and thermosyphon loop. The third section includes nanofluids for heat transfer, nanofluids in minichannels, potential and engineering strategies on nanofluids, and heat transfer at nanoscale. The forth section presents time-dependent melting and deformation processes of phase change material (PCM), thermal energy storage tanks using PCM, phase change in deep CO2 injector, and thermal storage device of solar hot water system. The advanced idea and information described here will be fruitful for the readers to find a sustainable solution in an industrialized society.

How to reference

In order to correctly reference this scholarly work, feel free to copy and paste the following:

Panagiotis Sismanis (2011). Modeling Solidification Phenomena in the Continuous Casting of Carbon Steels, Two Phase Flow, Phase Change and Numerical Modeling, Dr. Amimul Ahsan (Ed.), ISBN: 978-953-307-584-6, InTech, Available from: http://www.intechopen.com/books/two-phase-flow-phase-change-and-numerical-modeling/modeling-solidification-phenomena-in-the-continuous-casting-of-carbon-steels

INTECH
open science | open minds

InTech Europe
University Campus STeP Ri
Slavka Krautzeka 83/A
51000 Rijeka, Croatia
Phone: +385 (51) 770 447
Fax: +385 (51) 686 166
www.intechopen.com

InTech China
Unit 405, Office Block, Hotel Equatorial Shanghai
No.65, Yan An Road (West), Shanghai, 200040, China
中国上海市延安西路65号上海国际贵都大饭店办公楼405单元
Phone: +86-21-62489820
Fax: +86-21-62489821